Materials Today • Volume 20, Number 9 • November 2017

Highly enhanced and stable activity of defect-induced titania nanoparticles for solar light-driven CO_2 reduction into CH_4

Saurav Sorcar [1], Yunju Hwang [1], Craig A. Grimes [2], Su-Il In [1],*

[1] Department of Energy Science and Engineering, DGIST, 333 Techno Jungang-daero, Hyeonpung-myeon, Dalseong-gun, Daegu 42988, Republic of Korea
[2] Flux Photon Corporation, 116 Donmoor Court, Garner, NC 27529, United States

Photocatalytic reduction of CO_2 to fuel offers an exciting opportunity for helping to solve current energy and global warming problems. Although a number of solar active catalysts have been reported, most of them suffer from low product yield, instability, and low quantum efficiency. Therefore, the design and fabrication of highly active photocatalysts remains an unmet challenge. In the current work we utilize hydrogen-doped, blue-colored reduced titania for photocatalytic conversion of CO_2 into methane (CH_4). The photocatalyst is obtained by exposure of TiO_2 to $NaBH_4$ at 350 °C for 0.5 h. Sensitized with Pt nanoparticles, the material promotes solar spectrum photoconversion of CO_2 to CH_4 with an apparent quantum yield of 12.40% and a time normalized CH_4 generation rate of 80.35 μmol g^{-1} h^{-1}, which to the best of our knowledge is a record for photocatalytic-based CO_2 reduction. The material appears intrinsically stable, with no loss in sample performance over five 6 h cycles, with the sample heated in vacuum after each cycle.

Introduction

As is now well known, anthropogenic emission of greenhouse gases, particularly CO_2, is a significant factor driving global climate change [1]. Sustainable, low carbon, readily portable fuels are one of the most pressing needs of modern society. To that end, a number of studies have investigated conversion of CO_2 into products such as CH_4 [2], CH_3OH [3], and CO [4]. For this purpose, a variety of semiconductors have been studied, to cite but a few examples $ZnGa_2O_4$ [5], CdS [6], TiO_2 [6,7], and Ru/RuO_x loaded TiO_2 [8,9]. However, despite the many efforts, the photocatalysts studied to date suffer from low photoconversion efficiency and limited stability.

The surface structure of a photocatalyst plays a crucial role in determining photocatalytic activity. A recent report [10] suggests that creating oxygen vacancies (V_o) and Ti^{3+} states in titania results in an upward shift of the valence band maximum (VBM) and a downward shift of the conduction band maximum (CBM), in turn enhancing light absorption properties. In initial studies reduced titania has shown promising photocatalytic activity for H_2 generation by water photoelectrolysis [11] and CO_2 photoreduction [12]. Liu et al. studied the role of surface V_o and Cu species over reduced titania [4], and Zhu et al. synthesized Cu(I) supported titania nanosheets with defective {001} facets [10]. Pt, with a Fermi level (5.35–5.63 eV) more positive than that of titania (4.67–4.70 eV), might be expected to effectively promote CO_2 reduction [13]. However there are few reports on the photocatalytic performance of reduced titania sensitized with Pt nanoparticles, known to promote water-splitting and e^-–h^+ pair separation [12], in application to photocatalytic conversion of CO_2 to hydrocarbon fuels.

Herein, we report a facile low-temperature synthesis route for fabricating reduced titania nanoparticles blue in color. The photocatalyst, sensitized with Pt nanoparticles, is found to actively promote CO_2 photoreduction under solar spectrum light; with optimized samples we obtain a maximum CH_4 yield of 80.35 μmol g^{-1} h^{-1} and an apparent quantum yield (AQY) of 12.40%; see the Appendix for details of the AQY calculation. While variations on illumination (intensity, spectrum, duration) and sample conditions (planar or bulk samples, chamber size, static or dynamic conditions) make direct comparison difficult, it

---

* Corresponding author.
E-mail address: In, S.-I. (insuil@dgist.ac.kr).

1369-7021/© 2017 Elsevier Ltd. All rights reserved. https://doi.org/10.1016/j.mattod.2017.09.005

appears, to the best of our knowledge, that this is the highest rate of CO_2 to CH_4 solar spectrum photocatalytic conversion, and AQY, achieved to date.

Experimental

Synthesis of Blue Titania (BT)

200-mg P25 procured from Degussa, was ground with variable quantities of Sodium Borohydride ($NaBH_4$, 98%) procured from Alfa Aesar using a mortar and pestle, then placed in a quartz tube furnace and heated at 350 °C for 30 min under Ar flow. After annealing, the sample was washed with copious amounts of deionized (DI) water and then ethanol, a cycle repeated five times, and then dried at 90 °C in a vacuum oven for 12 h. Different reduced titania samples were prepared by varying the $NaBH_4$ amount (X), the samples, which are generally blue in color, denoted as BT-X, where $X = 20$, 30, 40 and 50 represents the amount of $NaBH_4$ used in milligrams, mg.

Photodeposition of Pt

Pt nanoparticles were photochemically deposited onto BT-30 samples in the following manner: 100 mg of sample BT-30 was added to 20-ml DI water and 5 ml CH_3OH (Duksan reagent). Variable concentrations of H_2PtCl_6 (HPLC grade, Sigma Aldrich) were added to the above mixture and stirred for 1 h under darkness in a closed system. The suspension was then irradiated with a 300 W Xe lamp (Newport) the light intensity of which was adjusted to 1 Sun (Air Mass (AM 1.5)) using a 1 Sun detector (Newport). The irradiation was performed for 2 h under mild stirring and the samples were then washed repeatedly with DI water, and finally dried at 90 °C in a vacuum oven for 12 h. The Pt photodeposited BT samples were named as Y-BT-30 (where $Y = 0.25$, 0.30, 0.32, 0.35, 0.42 and 0.50 corresponding to theoretically calculated wt. % Pt). In an identical manner 0.35 wt. % Pt was photodeposited upon comparative control samples. A control sample in which pure P25 was treated in Ar atmosphere, without $NaBH_4$ exposure, is identified as 0.35-P25 (Ar treated).

Photocatalyst characterization

X-ray diffraction (XRD) spectroscopy was performed on a Panalytical, Empyrean X-ray diffractometer using Cu kλ radiation ($\lambda = 1.54$ Å) operating at 40 kV and 30 mA. Raman analysis was carried out on a Raman Spectrometer, Nicolet Almeca XR, manufactured by Thermo Scientific. A 531 nm laser was used for excitation. The lattice structure of photocatalyst was visualized by a field emission transmission electron microscopy (FE-TEM) taken from Hitachi HF-3300 operating at 300 kV. The samples were dispensed upon Ni mesh grid with concentration of 0.05 mg/ml prepared in ethanol and allowed to dry overnight. ImageJ software was used to estimate the Pt nanoparticle size distribution and average particle size (d_{avg}) from the high resolution transmission electron microscopy (HR-TEM) images. The elemental composition and elemental mapping of 0.35-BT-30 (representative BT-30 sample with optimized Pt loading) were measured using the energy dispersive spectroscopy (EDS) attached with Hitachi HF-3300 FE-TEM. UV–visible diffuse reflectance spectra (UV–vis DRS) were measured using a Cary series UV–visible near infrared spectrophotometer with a diffuse reflectance accessory. Photoluminescence emission (PL) spectra were measured on a Cary Eclipse fluorescence spectrophotometer ($\lambda_{exc} = 320$ nm) of Agilent Technologies having a diffuse reflectance accessory. X-ray photoelectron spectroscopy (XPS) and valence band X-ray photoelectron spectroscopy (VB-XPS) were measured using Thermo VG, K-alpha using Al Kλ line (148606 eV) as the X-ray source. Electron paramagnetic resonance (EPR) spectra were recorded using a Jeol JES-FA100 spectrometer at 100 K. The N_2 sorption isotherms were measured at −196 °C on a BELSORP-miniII apparatus, with samples extensively degassed at 100 °C prior to the experiments. Surface areas were calculated by the Brunauer–Emmett–Teller (BET) equation. The pore volume was determined from the amount of N_2 adsorbed at the highest relative pressure of $(P/P_0) = 0.99$. Proton nuclear magnetic resonance (^{1}H NMR) measurement was recorded using a Bruker Avance 400 spectrometer.

Photocatalytic CO_2 reduction

Photocatalytic CO_2 reduction experiments were carried out using the experimental setup shown in Fig. 1. In brief, a 40 mg sample of the photocatalyst was evenly dispersed upon a porous fritted filter disc that was placed at the center of the photoreactor. Moist CO_2 gas was then continuously passed through the photoreactor at a flow rate of 40 ml/min. After 1 h purging the flow rate was decreased to 1.0 ml/min, and this rate was maintained for the entire photoreaction process. A 100 W Xe solar simulator (Oriel, LCS-100) with an AM1.5 filter was the light source. The concentration of the effluent gas, as a function of irradiation time, was analyzed every 30 min by a gas chromatograph unit (Shimadzu, GC-2014) equipped with an automated gas sampling valve, helium carrier gas, to determine CH_4 product yield (as shown in Eq. (1)) [14] from the photocatalytic system. The GC was equipped with a flame ionization detector (FID, Restek-Rt-Q-bond column, ID = 0.53 mm and length = 30 m). To evaluate photocatalyst stability, the photocatalyst was repeatedly tested for CO_2 photoreduction; after each 6 h test period the photocatalyst was vacuum annealed at 100 °C for 2 h, a process adopted from previous reports for regenerating used photocatalyst [15,16].

$$\text{Total } CH_4 \text{ yield}(\mu\text{mol}) = \frac{(C_{final,CH_4} - C_{initial,CH_4}) \times \text{volumetric flow of product gas}}{\text{Amount of photocatalyst used}\,(\text{g})} \qquad (1)$$

Control and $^{13}CO_2$ isotopic experiments were performed to investigate the origin of carbon involved in hydrocarbon generation. The control test was carried out in (i) $Ar/H_2O_{(g)}$ mixture instead of moist CO_2 with similar experimental conditions, and (ii) a blank reactor test without any photocatalyst. For isotopic experiments, $^{13}CO_2$ (^{13}C 99%) was purchased from Aldrich and diluted in pure He gas (99.999%) to give $^{13}CO_2$ with final a concentration of 1000 ppm in He. The $^{13}CH_4$ produced by moist $^{13}CO_2$ gas ($^{13}CO_2 + H_2O$ mixture) was analyzed using Gas chromatography–Mass spectrometer (GC–MS) manufactured by Shimadzu, GC–MS-QP2010 ultra (Restek Rt Q-bond column, ID = 0.32 mm and length = 30 m). Moist $^{13}CO_2$ was introduced into the photocatalyst (40 mg)-loaded, AM 1.5G illuminated photoreactor and the gaseous products analyzed after 1 h, 2 h, and 3 h.

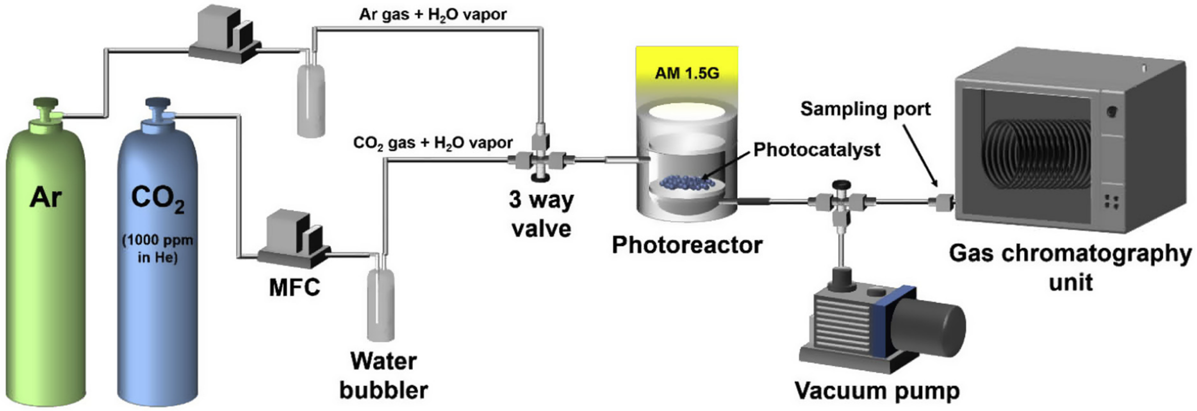

FIGURE 1

Setup used for the photocatalytic CO_2 reduction into CH_4 experiments, employing an online gas chromatography (GC) system for dynamic analysis of gaseous products.

Results and discussion

Powder X-ray diffraction patterns (XRD) of P25 [17] and blue titania (BT)-X, where X represents the amount of $NaBH_4$, in mg, used for reduction (0.5 h at 350 °C), are shown in Fig. 2a. The XRD patterns indicate no significant appearance of any new phase and/or any structural change during the reduction process. As the amount of $NaBH_4$ increases, the sample color changes from white, to light blue, to dark blue, suggesting defect formation within the titania nanoparticles (Fig. 2b). Fig. S1 shows the XRD patterns of various Pt-sensitized BT-30 samples. The size and content of the dispersed Pt nanoparticles is beyond the XRD detection limit, in agreement with previous reports [18,19].

Fig. 3a shows a HR-TEM image of P25, where well-defined lattice fringes are seen with a 0.35-nm spacing confirming its crystallinity [12]; an image of sample BT-30, Fig. 3b, shows a disordered shell ≈1–2 nm thick and a crystalline core; the structural difference is in accordance with Raman spectroscopy used to confirm V_o and non-stoichiometry, see Fig. S2. BT-30, which showed optimal photocatalytic CO_2 reduction activity, was sensitized with different amounts of co-catalyst Pt; such samples are identified as Y-BT-30 where $Y = 0.25$, 0.30, 0.32, 0.35, 0.42 and 0.50 corresponding to the theoretically calculated Pt wt. %. Fig. 3c exhibits a TEM image of sample 0.35-BT-30, in which well-dispersed Pt nanoparticles are evident; Fig. 3d is a magnified image of the region enclosed by the red circle in Fig. 3c. In Fig. 3d we see clear lattice fringes with interplanar distances of 0.35 nm and 0.23 nm, typical for the (1 0 1) plane of anatase [12,20] and (1 1 1) plane of face-centered cubic Pt [21]. Fig. 3e–h shows elemental mapping of sample 0.35-BT-30 with red, blue and green spots respectively assigned to Ti, O and Pt. The Gaussian curve, Fig. 3j, indicates that the Pt nanoparticles are well dispersed with an average size of 2.42 ± 0.05 nm.

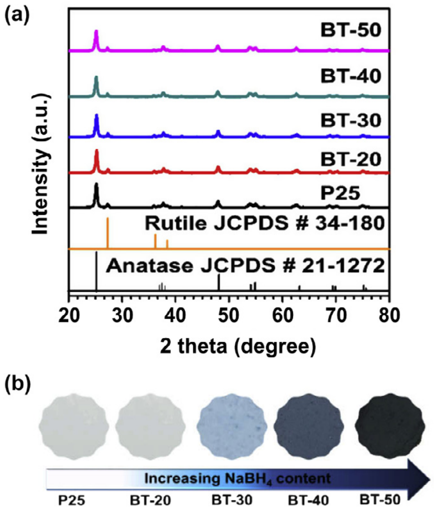

FIGURE 2

XRD patterns of: (a) different blue titania samples, and (b) depiction of color change for samples after reduction process with respect to amount of $NaBH_4$.

Textural properties of the samples were characterized by N_2 adsorption–desorption isotherms with the results provided as Figs. S3 and S4 for blue titania and Pt deposited blue titania samples, respectively. All BT samples possessed comparable BET surface areas of 52–56 $m^2\,g^{-1}$, see Table 1. A reduction in BET surface area of the Y-BT-30 samples was observed, indicating successful grafting of the Pt nanoparticles [21,22] see Fig. S4.

Fig. 4a displays UV–vis DRS spectra; all reduced titania samples exhibit significant amounts of light absorption in the visible region. Tauc plots are used to calculate the bandgap, see Fig. S5 and Table S1. The enhanced absorption is attributed to both disordered surface layers and trivalent titanium ions. It is known that hydrogen atoms in the amorphous layers can strongly interact with the Ti 3d and O 2p electrons, leading to a considerable decrease in the band gap ascribed to mid-gap states formation [23,24]. Further, hydrogenation causes disorder among the surface states inducing an upward shift of the valence band maximum [23,24], while Ti^{3+} and V_o reduce the conduction band minimum [23,24].

Fig. 4b compares the UV–vis DRS spectra of different Pt wt. % photodeposited BT-30 samples. The enhancement of visible light absorption with Pt sensitization is due to localized surface plasmon resonance (LSPR) [18,25]. Fig. 4c displays the comparative photoluminescence (PL) spectra of different reduced titania samples; PL emission results from the recombination of free charge

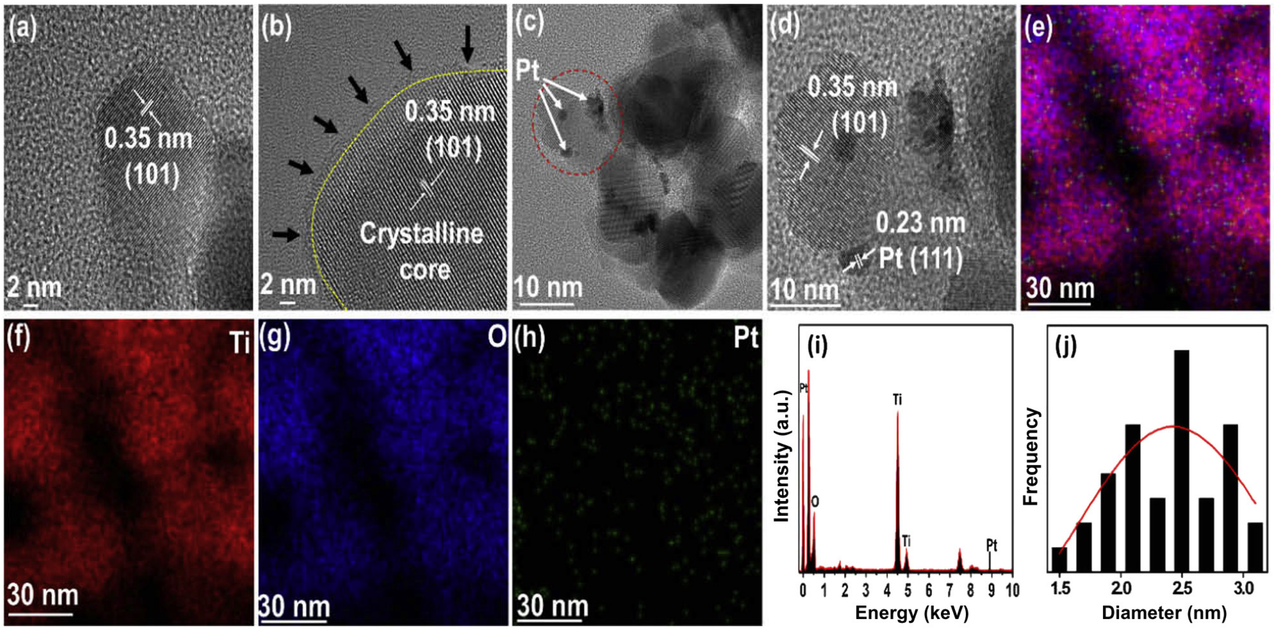

FIGURE 3

HR-TEM images of: (a) P25, (b) BT-30 where the arrows indicate a disordered shell, (c) 0.35-BT-30, (d) enlarged image of 0.35-BT-30. Elemental mapping for: (e) 0.35-BT-30, showing the regions of (f) Ti, (g) O, (h) Pt, (i) EDS, and (j) particle size distribution of the Pt nanoparticles in 0.35-BT-30.

TABLE 1

Physiochemical properties of photocatalysts.

Sample	Pt size (nm)	Pt content (atomic %, from ICP-OES)	BET (m^2 g^{-1})	Pore volume (cm^3 g^{-1})	CH_4 yield (μmol g^{-1} h^{-1})	AQY (%)
P25	–	–	56.50	0.28	–	–
BT-20	–	–	54.10	0.50	2.12	0.32
BT-30	–	–	55.70	0.49	2.79	0.41
BT-40	–	–	53.40	0.42	0.88	0.13
BT-50	–	–	52.10	0.40	0.68	0.10
0.25-BT-30	1.82 ± 0.07	0.18	49.3	0.38	10.16	1.52
0.30-BT-30	2.18 ± 0.04	0.22	46.4	0.35	20.03	3.08
0.32-BT-30	2.25 ± 0.02	0.28	45.9	0.34	48.96	7.53
0.35-BT-30	2.42 ± 0.05	0.33	45.5	0.32	80.35	12.40
0.42-BT-30	2.98 ± 0.06	0.38	44.7	0.31	66.68	10.32
0.50-BT-30	3.50 ± 0.18	0.42	43.9	0.30	41.13	6.34

carriers [22,23], thus reduced emissions can be interpreted as longer photogenerated charge lifetimes. Fig. 4d displays the PL spectra of different Pt wt. % sensitized BT-30 samples, with further quenching observed [13]. Electron paramagnetic resonance (EPR) and proton nuclear magnetic resonance spectroscopy (^{1}H NMR) was carried out to confirm the Ti^{3+} states and H doping in the blue titania samples, with the results and analysis given in Fig. S6a and b, respectively.

XPS was used to examine the effect of hydrogenation on the chemical composition and oxidation states. Fig. 5a shows the survey scan spectra of BT-30, with a high resolution scan of the Ti 2p region shown in Fig. 5b. For both samples two broad peaks centered at ~458.28 eV and ~464.08 eV are observed, corresponding to the characteristic Ti $2p_{3/2}$ and Ti $2p_{1/2}$ peaks of Ti^{4+} respectively [22,23]. In comparison to P25, the peaks of sample BT-30 show a negative shift in binding energy, suggesting that they have a different bonding environments [26]. The O 1s region, Fig. 5c, shows a similar shift of binding energy for BT-30, which suggests a transfer of electrons to neighboring V_o [27]. It should be noted that the generation of surface or subsurface V_o accompanies the formation of Ti^{3+} for charge compensation. XPS analysis was performed for all samples, see Fig. S7, and shows similar negative shifts in binding energy.

The density of states (DOS) were determined using valence band X-ray photoelectron spectroscopy (VB-XPS) [26,27], see Fig. 5d. P25 shows the characteristic valence band DOS of titania, with the band edge at ~2.29 eV (Fig. 4d). The VB-XPS of BT-30 had an absorption onset located at 1.19 eV, whereas the maximum energy associated with the band tail is blue-shifted to 1.10 eV (Fig. 4d); similar changes in DOS have been previously reported for reduced titania [26,27]. Fig. S8 shows the VB-XPS results and band energy diagrams for samples BT-20, BT-40, and BT-50; it is evident that the valence band tail increases with degree of reduction. The XPS spectra of 0.35-BT-30 and other Pt

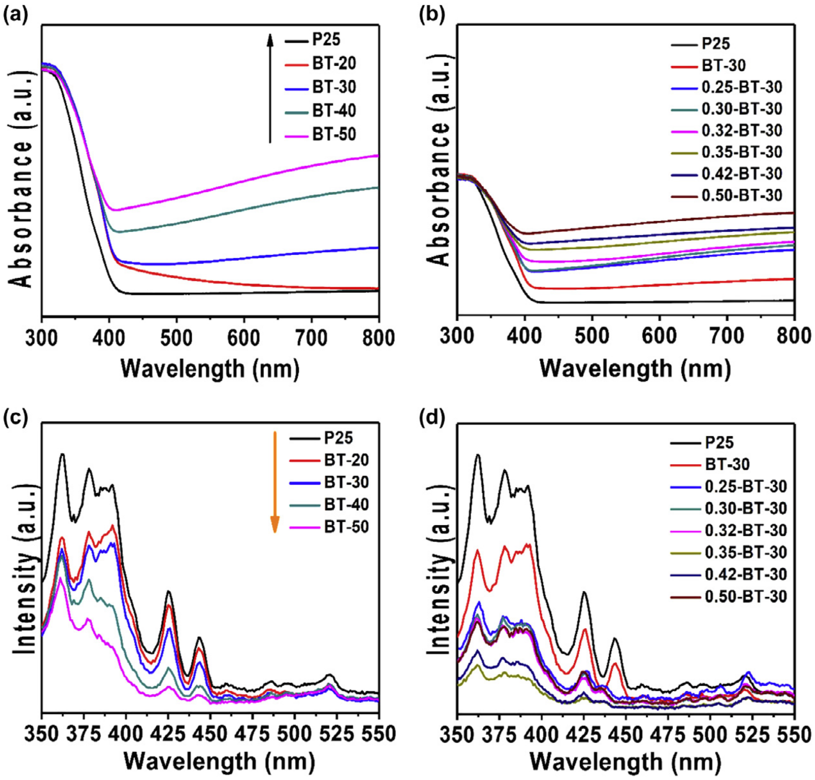

FIGURE 4

(a), (b) UV–vis DRS spectra, and (c), (d) PL spectra of different reduced titania samples, and different Pt wt. % photodeposited BT-30 samples, respectively.

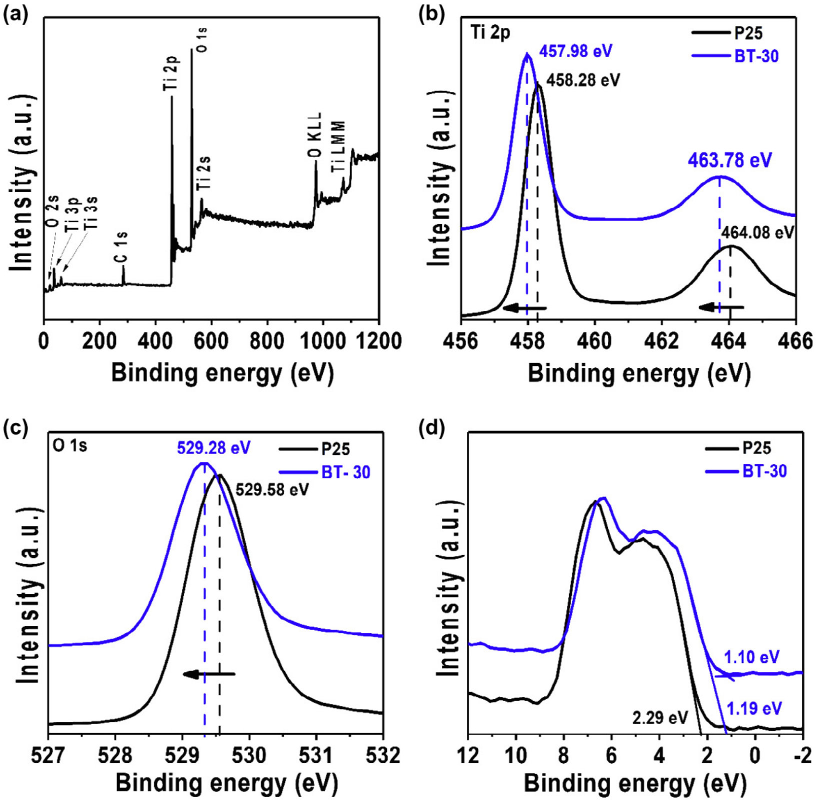

FIGURE 5

(a) Survey scan spectra of sample BT-30, (b) comparative core level XPS spectra of Ti 2p for BT-30 and P25 nanoparticles, (c) comparative core level XPS spectra of O 1s for BT-30 and P25 nanoparticles, and (d) comparative VB-XPS of BT-30 and P25 nanoparticles.

deposited reduced titania samples is given in Figs. S9 and S10 respectively, confirming the presence of Pt.

Gas phase photocatalytic CO_2 reduction results are shown in Fig. 6. According to GC analysis CH_4 was the predominant hydrocarbon product in all experiments, with vanishingly small amounts of ethane. The CH_4 evolution rate significantly increases with titania reduction, with a maximum CH_4 evolution rate of 2.79 $\mu mol\ g^{-1}\ h^{-1}$ (8.39 $\mu mol\ g^{-1}$) observed for sample BT-30. The decrease in activity seen for BT-40 and BT-50 is presumably due to excessive Ti^{3+}, which can serve as recombination centers for photogenerated charges [11,15,23].

It is well known that noble metals create electron sinks as well as active sites for photocatalytic CO_2 reduction [18,28]. As evident from the optical properties of the *Y*-BT-30 samples, Pt not only extends the photoresponse but also suppresses charge carrier recombination by facilitating interfacial electron transfer. Pt loading values were experimentally verified by ICP-OES analysis, and found to be quite close to theoretical calculations, Table 1.

The continuous CH_4 production profile and rate of CH_4 production for different Pt wt. % sensitized BT-30 under solar spectrum illumination are shown in Fig. 6b and c, respectively. Among the studied samples, the rate of CH_4 evolution reaches a maximum of 80.35 $\mu mol\ g^{-1}\ h^{-1}$ [482.12 $\mu mol\ g^{-1}$] for sample 0.35-BT-30 (6 h) (Fig. 6c). A maximum apparent quantum yield (AQY) of 12.40%, see Table 1, is achieved. As far as we know, the CH_4 production rate and AQY are the highest with regards to photocatalytic CO_2 reduction under solar illumination as compared with previous studies (Table S2). A small amount of ethane (C_2H_6) was also detected among the Pt photodeposited blue titania samples whose results have been reported in Table S3, along with the selectivity for each photocatalyst studied herein this work.

In comparison to 0.35-BT-30, a decrease in the CH_4 evolution and AQY was observed for 0.25-BT-30, 0.30-BT-30 and 0.32-BT-30. We suggest that the low Pt content did not provide sufficient electron trap centers to hinder charge recombination, resulting in a reduced photoactivity. Higher Pt content beyond our optimum sample also manifests a decreasing trend in CH_4 yield. Fig. S11 and Table 1 show, respectively, the size distribution and mean particle size of the Pt nanoparticles. Pt nanoparticle size increases with increasing Pt precursor concentration, varying from 1.82 nm for 0.25 Pt wt. %, to 3.5 nm for 0.50 Pt wt. %. It is known that energy levels shift upward in very small nanoparticles [13].

Catalyst stability is of utmost importance in realizing a practical system. Fig. 6d shows the stability of representative sample

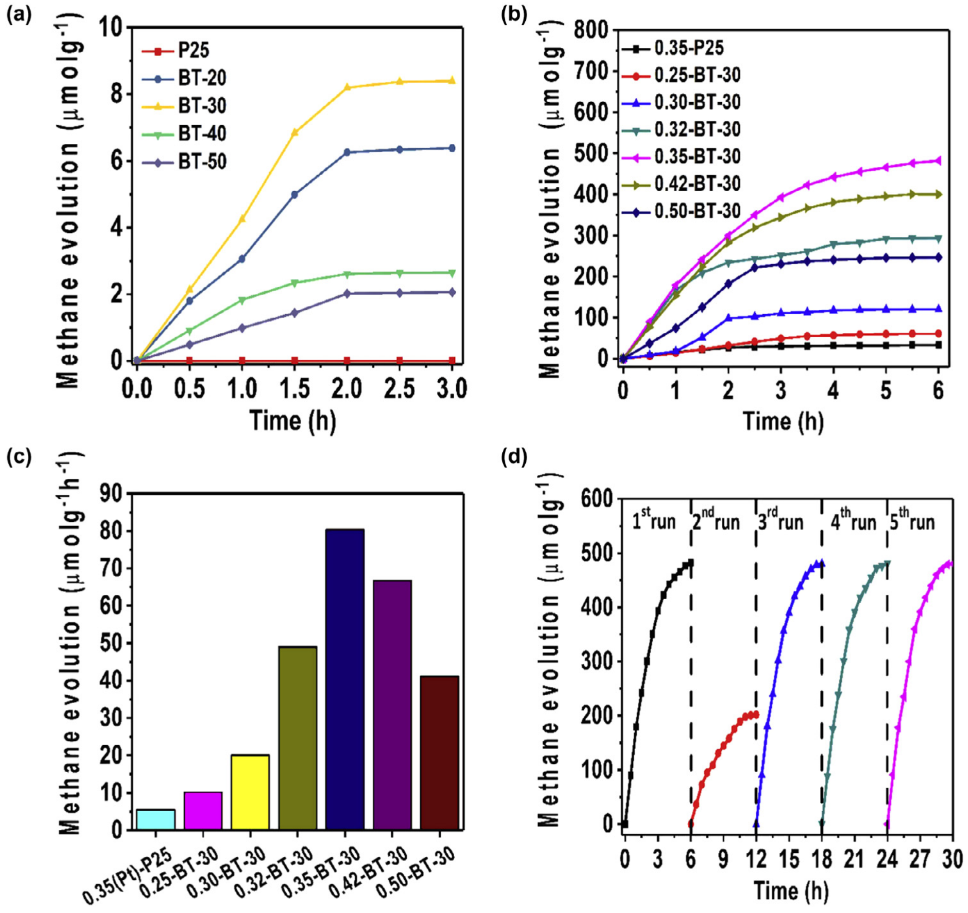

FIGURE 6

Photocatalytic CO_2 reduction results. Cumulative methane evolution under AM 1.5G illumination for: (a) P25 and reduced titania samples, and (b) *Y*-BT-30 samples. (c) Evolution amounts of CH_4 in the first 6 h irradiation from photocatalytic CO_2 conversion for different Pt-sensitized BT-30. (d) Stability test of 0.35-BT-30; at the end of 2nd, 3rd and 4th cycle the photocatalyst is placed within a vacuum oven at 100 °C for 2 h.

0.35-BT-30 upon sequential testing. The decrease in production rate during the second cycle (without thermo-vacuum treatment) suggests a gradual deactivation of the photocatalyst, a phenomenon commonly observed in CO_2 photoreduction studies [14,29] and believed due to saturation of adsorption sites on the titania surface with intermediate products [14,29]. However, the photocatalyst recovers its activity after being heated in a vacuum oven at 100 °C for 2 h after 2nd, 3rd and 4th run. We have also conducted the stability tests with a separate fresh batch of 0.35-BT-30 sample, and it also shows a similar methane yield and sample stability, thus confirming the reproducibility in methane yield (Fig. S12).

To help rule out possible involvement of carbon impurities or surface contaminants, a photoconversion test was run using a mixture of $Ar_{(g)}$ and H_2O, and the reactor was illuminated in the presence of moist CO_2 but in the absence of photocatalyst. For both tests the measurable CH_4 yield was negligible, see Fig. 7a.

A ^{13}C-labeled isotopic experiment was performed, using $^{13}CO_2$ instead of standard $^{12}CO_2$, with the resulting $^{13}CH_4$ analyzed by GC-MS, see Fig. 7b–d. Fig. 7b corresponds to $^{13}CO_2$, while Fig. 7c shows the signal at $m/z = 17$ attributed to $^{13}CH_4$ [15,30–32] confirming CO_2 as the main carbon source for CH_4 generation. We conducted prolonged photocatalytic isotopic tests, Fig. 7d, finding an increase in $^{13}CH_4$ from 1 h to 3 h. A similar observation in increase of isotopic gaseous products with prolonged illumination was reported previously [33]. Figs. S13–S15 show optical properties and CO_2 photoreduction results of various control samples, respectively.

Literature suggests the process of CO_2 photoreduction is based on proton coupled multi-electron transfer [13,15,34–41]. Work by Thampi et al. have elucidated the underlying mechanism to generate CH_4 from CO_2 photoreduction, where electrons and holes created in the TiO_2 bandgap play a key role in the methanation process [8]. To produce H^+ ions the VBM should be at a potential more positive than that of H_2O/O_2 [34], while the CBM should be more negative than the CH_4/CO_2 potential. For BT-30, UV–vis DRS analysis indicates a band gap of 2.73 eV. From the VB-XPS results as shown in Fig. 8a, the VBM position for BT-30 is at 1.19 eV which is more positive than $E_o(H_2O/O_2)$ (0.82 V *vs.* NHE). The CBM is located to be at −1.54 eV which is more negative than $E_o(CH_4/CO_2)$ (−0.24 V *vs.* NHE).

Under illumination, photogenerated e^-–h^+ pairs are generated in the CB and VB of the BT, (reaction 2); the electrons can transfer to the Pt nanoparticles due to the lower Fermi energy level [13]. The holes in the valence band can oxidize adsorbed H_2O into O_2 and protons (H^+) because the VBM position is more positive than that of $E_o(H_2O/O_2)$ [15,20,30,34,41–46] (reaction 3). The formation of CH_4 requires $8e^-$ and $8H^+$. The enriched e^- density on the Pt nanoparticles would favor CH_4 formation, which is thermodynamically more feasible than CO, by transfer of e^- from the CBM of BT-30 to Pt, and from there to surface

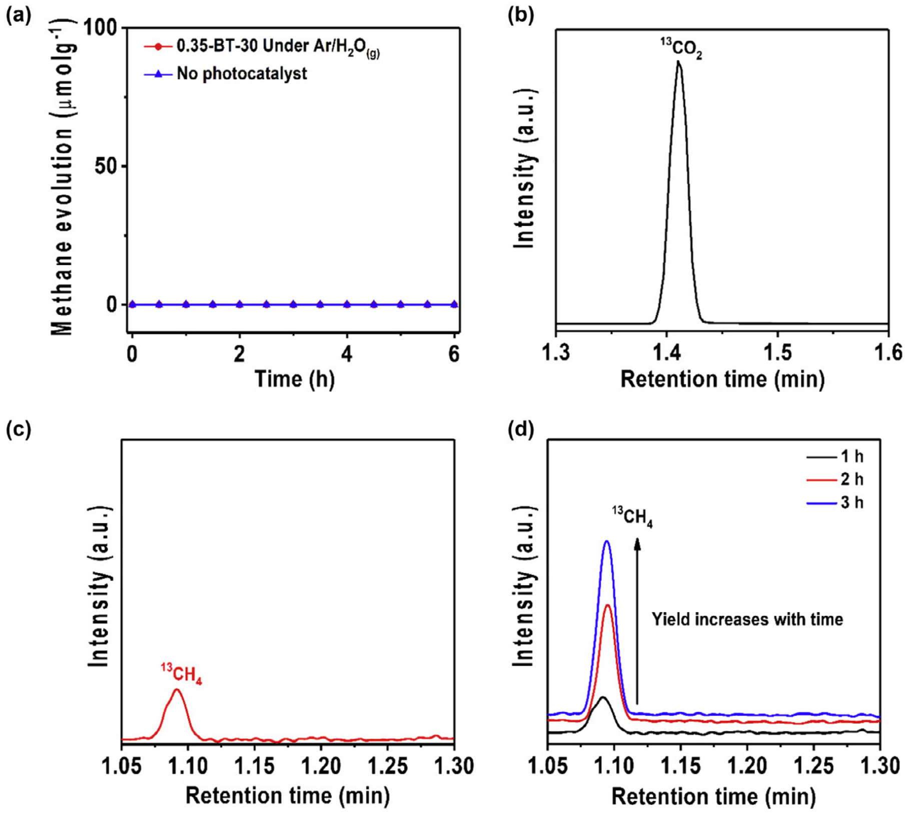

FIGURE 7

(a) Control test results of sample 0.35-BT-30. GCMS spectrum of: (b) $^{13}CO_2$ used during the experiment; (c) $^{13}CH_4$ produced from 0.35-BT-30 in 1 h; and (d) $^{13}CH_4$ evolved during prolonged photocatalytic testing of 0.35-BT-30 under moist $^{13}CO_2$ atmosphere.

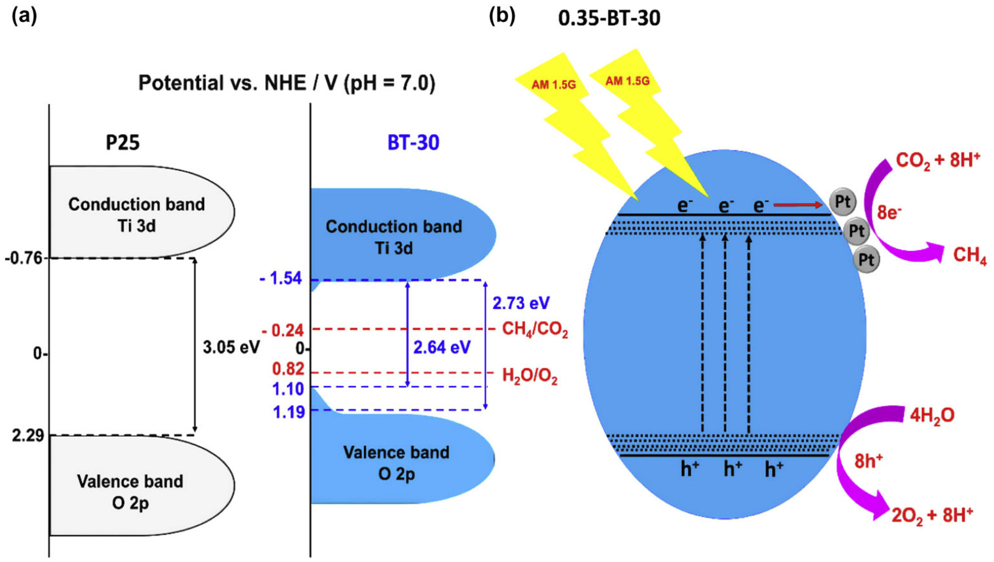

FIGURE 8

(a) Proposed energy band diagram of P25 nanoparticles and sample BT-30, and (b) possible transfer of electrons in 0.35-BT-30 under AM 1.5G illumination for photoreduction of CO_2 into CH_4.

adsorbed CO_2 molecules [18] (reaction 4). Fig. 8b illustrates a possible mechanism by which CO_2 could be photoconverted into CH_4, based upon our experimental results for 0.35-BT-30.

$$\text{Pt-BT} + h\nu \rightarrow \text{Pt-BT}(\text{Ti}^{3+}e^-_{CB}) + \text{Pt-BT}(\text{V}_o h^+_{VB}) \qquad (2)$$

$$4H_2O + \text{Pt-BT}(V_o 8h^+_{VB}) \rightarrow 8H^+ + 2O_2 \qquad (3)$$

$$CO_2 + 8H^+ + \text{Pt-BT}(\text{Ti}^{3+}8e^-_{CB}) \rightarrow CH_4 + 2H_2O \qquad (4)$$

4. Conclusions

A rapid, low-temperature technique for reducing titania was developed; the H_2 desorbed from $NaBH_4$ create oxygen vacancies changing the valence of Ti^{4+} to Ti^{3+}. Physiochemical and optical properties of the blue titania were analyzed, and a photocatalyst with optimum defects, narrow band gap, well-aligned band position, and reduced charge recombination for photocatalytic CO_2 reduction into CH_4 was obtained. The loading of a small amount of Pt (0.35 wt. %) onto the blue titania samples was found to significantly enhance CH_4 production, showing an increase of 29× over the pristine blue titania. As revealed by ICP-OES and HR-TEM analysis, it was found that both the size and quantity of the Pt nanoparticles play a key role in determining photocatalytic efficiency. The maximum CH_4 production rate obtained was 80.35 $\mu mol\ g^{-1}\ h^{-1}$ under simulated solar light, a value superior to those of previously reported photocatalyst materials. After undergoing desorption, the catalyst shows appreciable stable performance over five 6 h cycles, the limit of our testing. Several control tests and a ^{13}C isotopic tracer experiment were conducted to confirm CO_2 as the carbon source. The outstanding activity and stability of our reduced titania samples suggest that a balanced combination of surface defects, oxygen vacancies, band position, and optimized amount of Pt cocatalyst enables an efficient photocatalyst for photoconversion of CO_2 to fuel.

Acknowledgments

The authors gratefully acknowledge the support of the DGIST R&D Program of the Ministry of Science and ICT (17-01-HRLA-01). This research was also supported by the Technology Development Program to Solve Climate Changes of the National Research Foundation (NRF) funded by the Ministry of Science and ICT (NRF-2015M1A2A2074670).

Appendix A. Supplementary data

Supplementary data associated with this article can be found, in the online version, at https://doi.org/10.1016/j.mattod.2017.09.005.

Appendix B. Apparent quantum yield (AQY) calculation

Apparent quantum yield (AQY) is defined as the ratio of number of reacted electrons to the number of incident photons. The general equation is given as below [13,47,48]

$$\text{AQY}\ (\%) = \frac{Number\ of\ reacted\ electrons}{Number\ of\ incident\ photons} \times 100 \qquad (A.1)$$

As given in equation (A.2), during the photocatalytic CO_2 reduction, stoichiometrically 8 electrons are required to produce one molecule of CH_4 [13]

$$CO_2 + 8H^+ + 8e^- \rightarrow CH_4 + 2H_2O \qquad (A.2)$$

Therefore, number of reacted electrons can be calculated by directly multiplying 8 with mole of CH_4 produced during the photocatalytic reaction [13]

$$\text{Number of reacted electrons} = [CH_4] \times 8 \times N_A \qquad (A.3)$$

where $[CH_4]$ represents mole of CH_4 produced in time (t) and N_A is the Avogadro's number ($6.022 \times 10^{23}\ mol^{-1}$). Herein, we describe the calculation for 0.35-BT-30 sample, which yield 80.35 $\mu mol\ g^{-1}\ h^{-1}$ CH_4.

Therefore,

$$\boldsymbol{number\ of\ reacted\ electrons} = \mathbf{3.87 \times 10^{20}} \tag{A.4}$$

The number of incident photons is same as the photon flux density [49], which is given by Eq. (A.5)

$$Number\ of\ incident\ photons = \frac{Light\ absorbed\ by\ the\ photocatalyst}{The\ average\ photon\ energy} \times t \tag{A.5}$$

where "*t*" is the photoreaction time (s). Thus, light absorbed by the photocatalyst is given by:

$$\boldsymbol{Light\ absorbed\ by\ the\ photocatalyst} = \boldsymbol{H} \times \boldsymbol{A} = \mathbf{0.49 Js^{-1}} \tag{A.6}$$

H is the apparent light input at the photocatalyst (Wm^{-2}) of 100 W xenon solar simulator (Oriel, LCS-100) with an AM 1.5 filter used in the present study ($H = 1000\ Wm^{-2}$) [13,50,51]. Similar assessments were reported by Grätzel et al. [52]. A represents the geometric irradiation area of the photocatalyst placed inside the photoreactor, which is 0.00049 m^2.

$$\boldsymbol{The\ average\ photon\ energy\ is\ given\ by} = \frac{\boldsymbol{hc}}{\lambda} = \mathbf{5.64 \times 10^{-19} J} \tag{A.7}$$

where h is Planck's constant ($h = 6.626 \times 10^{-34}$ Js), $c = 3 \times 10^8\ ms^{-1}$ and the value of λ is found as average wavelength of the broadband light source (352 nm). Since the bandgap of BT-30 as estimated from Tauc plot analysis is 2.73 eV, therefore, unbound and free electron-hole pairs cannot be generated for $\lambda > 454$ nm. Thus, photons with wavelength 250–454 nm can excite electrons, whose average photonic wavelength ($\lambda = 352$ nm) is used to calculate the apparent quantum efficiency [51,53].Combining values from Eqs. (A.6) and (A.7) and substituting in Eq. (A.5)

$$\boldsymbol{Number\ of\ incident\ photons} = \mathbf{3.12 \times 10^{21}} \tag{A.8}$$

Substituting values from (A.4) and (A.8) in Eq. (A.1), the AQY of sample 0.35-BT-30 is found to be 12.40%. The AQY values for all samples are given in Table 1.

References

[1] M.I. Hoffert et al., Science 298 (2002) 981–987.
[2] K. Kim et al., RSC Adv. 6 (2016) 38964–38971.
[3] D.C. Grills, E. Fujita, J. Phys. Chem. Lett. 1 (2010) 2709–2718.
[4] L. Liu, C. Zhao, Y. Li, J. Phys. Chem. C 116 (2012) 7904–7912.
[5] S.C. Yan et al., Angew. Chem. Int. Ed. 122 (2010) 6544–6548.
[6] V.P. Indrakanti, J.D. Kubicki, H.H. Schobert, Energy Environ. Sci. 2 (2009) 745–758.
[7] S. In et al., J. Am. Chem. Soc. 129 (2007) 13790–13791.
[8] R. Thampi, J. Kiwi, M. Graetzel, Nature 327 (1987) 506–508.
[9] R. Thampi, L. Lucarelli, J. Kiwi, Langmuir 7 (1991) 2642–2648.
[10] S.Y. Zhu et al., Phys. Chem. Chem. Phys. 17 (2015) 9761–9770.
[11] A. Sinhamahapatra, J. Jeon, J. Yu, Energy Environ. Sci. 8 (2015) 3539–3544.
[12] J. Zhao et al., Appl. Catal. A: Gen. 510 (2016) 34–41.
[13] W.N. Wang et al., J. Am. Chem. Soc. 134 (2012) 11276–11281.
[14] W.J. Ong et al., RSC Adv. 3 (2013) 4505–4509.
[15] A. Razzaq et al., Appl. Catal. B: Environ. 215 (2017) 28–35.
[16] M. Li et al., Nano Energy 19 (2016) 145–155.
[17] S. Docao et al., Energy Environ. Sci. 10 (2017) 628–640.
[18] Y. Wang et al., RSC Adv. 4 (2014) 44442–44451.
[19] T.A. Kandiel, A.A. Ismail, D.W. Bahnemann, Phys. Chem. Chem. Phys. 13 (2011) 20155–20161.
[20] S.-I. In, D.D. Vaughn, R.E. Schaak, Angew. Chem. Int. Ed. 51 (2012) 3915–3918.
[21] B. Banerjee et al., Nanoscale 7 (2015) 10504–10512.
[22] D.S. Kim, J.D. Jeon, K.H. Shin, Microporous Mesoporous Mater. 181 (2013) 61–67.
[23] Z. Wang et al., Adv. Funct. Mater. 23 (2013) 5444–5450.
[24] R. Fu et al., RSC Adv. 4 (2014) 37061–37069.
[25] Y. Shan et al., RSC Adv. 5 (2015) 34737–34743.
[26] M. Senna et al., J. Solid State Chem. 187 (2012) 51–57.
[27] Y. Yan et al., J. Mater. Chem. A 2 (2014) 12708–12716.
[28] W. Ong et al., Dalton Trans. 44 (2015) 1249–1257.
[29] L. Liu et al., Appl. Catal. B: Environ. 134–135 (2013) 349–358.
[30] T. Yui et al., ACS Appl. Mater. Interfaces 2 (2011) 2594–2600.
[31] S. Zhu et al., Green Chem. 18 (2016) 1355–1363.
[32] X. Meng et al., Chem. Commun. 50 (2014) 11517–11519.
[33] K. Li et al., Nanoscale 6 (2014) 9767–9773.
[34] S.N. Habisreutinger, L. Schmidt-Mende, J.K. Stolarczyk, Angew. Chem. Int. Ed. 52 (2013) 7372–7408.
[35] S.M. Park et al., ACS Omega 1 (2016) 868–875.
[36] K. Mori, H. Yamashita, M. Anpo, RSC Adv. 2 (2012) 3165–3172.
[37] B. Fang et al., ACS Sustain. Chem. Eng. 3 (2015) 2381–2388.
[38] H. Liu et al., Langmuir 32 (2015) 254–264.
[39] J.C. Wang et al., ACS Appl. Mater. Interfaces 8 (2016) 3765–3775.
[40] L. Yu, ACS Catal. 6 (2016) 6444–6454.
[41] L. Tan et al., Appl. Catal. B: Environ. 166–167 (2015) 251–259.
[42] M. Li et al., Appl. Catal. B: Environ. 201 (2017) 629–635.
[43] S. Zhu et al., Appl. Catal. B: Environ. 187 (2016) 11–18.
[44] J. Hou et al., Nano Energy 30 (2016) 59–68.
[45] G. Yang et al., Appl. Catal. B: Environ. 219 (2017) 611–618.
[46] X. Liu et al., Sci. Rep. 6 (2016) 38474.
[47] L. Tan et al., Chem. Eng. J. 308 (2017) 248–255.
[48] W.J. Ong et al., Nano Res. 7 (2014) 1528–1547.
[49] Y. Ding, P. Nagpal, Nanoscale 8 (2016) 17496–17505.
[50] H. Rim et al., J. CO_2 Util. 20 (2017) 91–96.
[51] M. Zubair et al., J. CO_2 Util. 20 (2017) 301–311.
[52] M. Schreier et al., Nat. Energy 2 (2017) 17087.
[53] W. Ong et al., Nano Energy 13 (2015) 757–770.